Soft Matter

PAPER

View Article Online
View Journal | View Issue

Cite this: *Soft Matter*, 2017, **13**, 8120

Smectic monolayer confined on a sphere: topology at the particle scale

Elshad Allahyarov, †*[abc] Axel Voigt[d] and Hartmut Löwen[a]

Received 24th August 2017,
Accepted 16th October 2017

DOI: 10.1039/c7sm01704a

rsc.li/soft-matter-journal

The impact of topology on the structure of a smectic monolayer confined to a sphere is explored by particle-resolved computer simulations of hard rods. The orientations of the particles are tangential to the sphere and either free or restricted to a prescribed director field with a latitude or longitude orderings. Depending on the imprinted topology, a wealth of different states are found including equatorial smectic with isotropic poles, equatorial smectic with empty poles, a broken egg-shell like modulated smectic, a capped nematic with equatorial bald patches, equatorial nematic with empty poles, and a situation with 4 or 8 half-strength topological defects. Potentially these states could be verified in experiments with Pickering emulsions of droplets with colloidal rods. The unique nature of dipolar structures consisting of positive and negative half-strength disclinations is revealed. These structures, classified by their density and interaction with other defects in the system, relieve the strain of the poles by separating closely positioned half-strength defects. The proximity of these structures to the half-strength defects might enhance the structural diffusion of the defects across the system.

1 Introduction

Liquid crystals composed of particles with orientational degrees of freedom typically exhibit phase diagrams with complex mesophases and show a plethora of novel effects in confinement[1–6] which are interesting both from a fundamental point of view[7] and for optical switching applications.[8] One important mesophase is the smectic state which involves a one-dimensional ordered stack of disordered layers. This liquid-crystalline phase can be stable in three[9,10] or two spatial dimensions,[11] the latter constituting a smectic monolayer. Particle-resolved computer simulations of simple models such as hard rods have largely contributed to our understanding of smectic phase stability. Complex confinement can induce a curvature of the smectic layers at the expense of elastic distortion energy[7] which is anisotropic and therefore highly nontrivial.

While the effect of curvature on nematic states has widely been studied under various complex boundary conditions,[12–22] only little theoretical studies have focused on smectics near curved walls[23,24] or on curved smectic shells.[20,25,26] The latter typically start from the phenomenological Landau–de Gennes free energy for an inhomogeneous smectic phase[27] which incorporates bent smectic layers.

In this letter, we focus on a particle-resolved view of a strongly curved smectic monolayer on a sphere. Our motivation to do so is fivefold: first, a confinement on a compact manifold will induce topological constraints for the orientational field. This is even more complex if the orientations are imposed with a fixed prescribed orientational field that contains topological defects. The role of topology on the defect formation in a smectic monolayer is expected to be dramatic. Second, we focus here on a particle-resolved view which include fluctuations which are ignored on the phenomenological mean-field level. They are naturally included in simulations at densities away from densest packing.[28] Third, smectic layers are realizable in experiments in various ways: by a double emulsion of a single[29] or two concentric droplets[30] filled with a molecular or colloidal smectic,[31–33] by smectic bubbles,[34–36] by freely suspended smectic films,[37–39] by vesicles formed from block copolymers with liquid-crystalline side chains,[40–42] and by air bubbles covered with rod-like nanoparticles.[43] Fourth, membrane morphologies in living cells, including membrane sculpting and tubulation, are regulated by proteins containing a Bin/Amphiphysin/Rvs domain, which consists of a banana-shaped rods.[44,45] Finally, the sickle-cell anemia disease is caused by a crowding of rod-like abnormal hemoglobin mutants in red-blood cells.[46] These conceptions also challenges a deeper fundamental understanding of rods on curved objects.

[a] *Institut für Theoretische Physik II: Weiche Materie, Heinrich-Heine Universität Düsseldorf, Universitätstrasse 1, 40225 Düsseldorf, Germany*
[b] *Theoretical Department, Joint Institute for High Temperatures, Russian Academy of Sciences (IVTAN), 13/19 Izhorskaya Street, Moscow 125412, Russia*
[c] *Department of Physics, Case Western Reserve University, Cleveland, Ohio 44106-7202, USA. E-mail: elshad.allahyarov@case.edu*
[d] *Institute of Scientific Computing, Technical University Dresden, D-01062 Dresden, Germany*
† Present address: Theoretical Chemistry, Duisburg-Essen University, Universitätsstrasse 5, 45141 Essen, Germany.

Ordered structures on spherical interfaces always possess topological defects.[29,47–49] The polar singularities of the defects can be functionalized by molecules, nanorods, polymers, lipids and other linkers to create directional bonds akin to atomic bonds.[50–52] The resulting colloidal spheres with anisotropic interactions can be used for fabrication of mesoscale particles such as nanoparticle chains, self-standing films, or diamond like structures from tetravalent mesoatoms with sp^3-like directional bonding.

Here, we study the impact of topology on the structure of a smectic monolayer confined to a sphere by particle-resolved computer simulations of hard rods. The orientations of the particles are always tangential to the sphere. We consider two situations where the orientation can freely rotate or are restricted to a prescribed director field. The latter is either along the lines of longitude, or along the lines of latitude. For the two imprinted orientations, two integer defects at the poles are imposed with expected huge impact on the smectic structure. Depending on the imprinted topology, a wealth of different states are found depending on rod area fraction, aspect ratio and sphere diameter. These include equatorial smectic with isotropic poles, equatorial smectic with empty poles, a broken egg-shell like modulated smectic, a capped nematic with equatorial bald patches, equatorial nematic with empty poles, and a situation with 4 or 8 half-strength topological defects. Potentially all of these structures could be verified in experiments with various set-ups mentioned above. We also focus on the nature of dipolar structures consisting of positive and negative half-strength defects. These structures are classified by their density and interaction with other defects in the system. In high density systems they relieve the strain of the poles by separating closely positioned half-strength defects. In low density systems, they are capable to enhance the structural diffusion of half-strength defects across the system.

The remainder of this paper is structured as follows. The details of our simulation model for the spherocylinders anchored on a spherical surface are given in Section 2. In Section 3 the simulation method is outlined. In Section 4 we describe three different prescribed orientations in the system of rods. The protocol of reaching high-density states, where the nematic to smectic transitions take place, is described in Section 5. We discuss the density modulations in smectic phases on a spherical surface in Section 6. Simulation results and the defect analysis for preordered and relaxed systems are gathered in Section 7. We conclude in Section 8.

2 The model

We consider N hard-core spherocylinders of cylindrical length L, width D, and the aspect ratio L/D anchored on the spherical surface S_2 of diameter $2R$. The particle–particle excluded volume interaction is defined as

$$u_{ij}\left(\vec{r}_{ij},\hat{\Omega}_i,\hat{\Omega}_j\right)=\begin{cases}\infty & \text{if } i \text{ and } j \text{ overlap,}\\ 0 & \text{otherwise.}\end{cases} \quad (1)$$

where the solid angle $\hat{\Omega}=\hat{\Omega}(\theta,\varphi)$ describes the particle orientation given by the spherical azimuthal angle φ and the polar angle θ. The system set-up is schematically shown in Fig. 1. In the simulations we fix the spherical surface radius to $R = 40D$. The anchoring position for the i-th particle on S_2 is given by its radius-vector $\vec{R}_i$ which points from the center of the sphere to the geometrical center of the spherocylinder. The anchoring is imposed by maintaining the center of the spherocylinder on the surface of the sphere at all times, $|\vec{R}_i| = \mathrm{R}$. The orientation of the spherocylinder at the position $\vec{R}_i$ is given by a unit vector $\vec{n}_i$, which is directed along the long axis of the spherocylinder and is perpendicular to $\vec{R}_i$. It is convenient to associate $\vec{n}_i$ with the angle ω_i defined as the angle in a clockwise rotation from the angular vector $\vec{e}_\theta$, which is tangential to the meridian at the point $\vec{R}_i$, $\vec{e}_\theta = \vec{R}_i \times [\vec{e}_z \times \vec{R}_i]$, to the vector $\vec{n}_i$. Here $\vec{e}_z$ is a unit vector along the axis z, and the angle ω_i obeys $\cos\omega_i = (\vec{n}_i\cdot\vec{e}_\theta)$. The vectors $\vec{e}_\theta$ and $\vec{n}_i$, and the angle ω_i are shown schematically in Fig. 1.

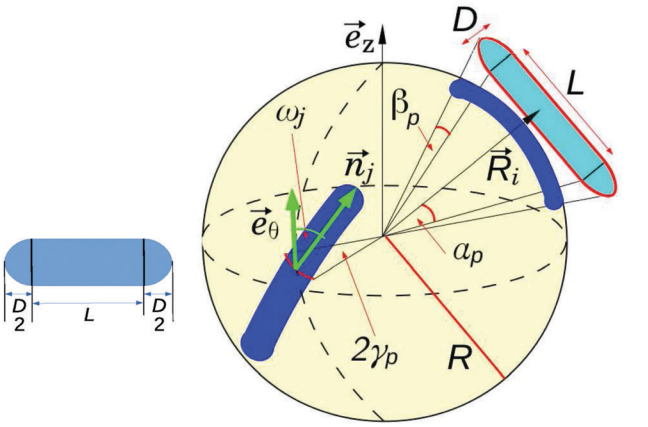

Fig. 1 Left picture: A spherocylinder of length L and diameter D. Right picture: A projection of spherocylinder with index i on the spherical surface S_2. The angle α_p is the projection angle between the tip of the rod and its center, β_p is the angle between the tip of the spherocylinder and the tip of the rod, $2\gamma_p$ is the angle related to the width D of the rod. Corresponding expressions for α_p, β_p, and γ_p are given in the text. The orientation parameters $\vec{n}_j$ and ω_j are shown separately for the spherocylinder with index j.

Each spherocylinder occupies an area S_p on S_2 defined as

$$S_p = 2R^2(2\alpha_p \sin\gamma_p + \pi(1-\cos\beta_p)) \quad (2)$$

where the angles α_p, β_p, and γ_p, shown in Fig. 1, are defined as follows: $\tan\alpha_p = L/(2R)$, $\tan\gamma_p = D/(2R)$, and $\tan\beta_p = \left[\frac{2R}{D}+\frac{L}{2R}\left(\frac{L}{D}+1\right)\right]^{-1}$. The area S_p can be viewed as the area of the projection of the spherocylinder on S_2. A curvature factor $\psi(L/R) = S_p/S_{2D}$, where S_{2D} is cross-section area of the spherocylinder, $S_{2D} = LD + \pi D^2/4$, can be introduced which depends on the curvature parameter L/R and measures the ratio between the projected and actual areas of the spherocylinder, $\psi(L/R) = 1$ for $R \to \infty$.

The areal packing fraction of the spherocylinders on S_2 reads

$$\eta = \frac{NS_p}{\pi(2R+D)^2} \quad (3)$$

In the limit of flat surface, $R \to \infty$, this parameter has the following asymptotics,

$$\eta^{\mathrm{AA}} = \frac{S_{2D}}{(L+D+a)(D+b)}, \qquad \eta^{\mathrm{AB}} = \frac{S_{2D}}{L(D+b)+(D+b)^2\sqrt{3}/2} \tag{4}$$

depending on what type of stacking, AA or AB is considered in the crystal phase. In eqn (4) b is the separation distance between the spherocylinders in the same layer, and a is the gap between neighboring layers. In the crystal phase the AA packing is maximal for $a = b = 0$ and $\eta^{\mathrm{AA}}(a=b=0) = \frac{L/D+\pi/4}{L/D+1}$ which varies between 0.96 to 0.99 for L/D changed from 4 to 24. Similarly the AB crystal has maximal packing for $b = 0$, $\eta^{\mathrm{AB}}(b=0) = \frac{L/D+\pi/4}{L/D+\sqrt{3}/2}$, which varies between 0.97 and 0.99 for L/D from 4 to 24. Multiplying these numbers by the curvature factor $\psi(L/R)$ of the sphere of radius $R = 40D$ we get $\eta^{\max} \approx 0.95$ for these two phases on the sphere for $4 < L/D < 24$. In other words, for the spherical geometry the packing fraction can reach the maximum value $\eta = 0.95$ in the crystal phase. According to data available in ref. 10, 53 and 54, the lower boundary of the smectic phase at the smectic–nematic transition is about 25–30% below its upper boundary at the smectic-columnar phase for $L/D \geq 5$. Projecting those results to the current study, it seems safe to expect that the smectic phase will be stable within a 20% window below the maximal value $\eta = 0.95$. Therefore, for obtaining a smectic phase, the simulations should be carried out for dense systems where the packing fraction is at least $\eta \geq 0.75$. Covering the spherical surface S_2 up to this packing number with overlap-free configuration of spherocylinders is a challenging task and demands the implementation of particular steps. This issue is discussed in the next section.

We will analyze the topology of the defect structures as a function of the packing fraction η and the aspect ratio L/D, see Appendix B for more details on the defect topology. The full defect structure will be discussed using the coding $t\mathrm{P}^{ijk}_{lmn}$. Here t is the total number of full- and half-strength defects recognized on the sphere, P denotes the phase in which the defect was observed, it takes values S for a smectic phase and N for the nematic phase, i is the number of full defects with a charge $s = 1$ and an angular phase $\gamma_s = 0$ (the parameters s and γ_s are defined in Appendix B), j is the number of full defects with a charge $s = 1$ and an angular phase $\gamma_s = \pi/2$, k is used for additional structural information about the defect such as iso caps on the spherical surface ($k = c$), or, bald patches on S_2 ($k = p$), or, periodic in-layer modulations in the smectic phase ($k = m$), l is the number of ++ defect pairs with a charge $s = 1/2$ and an angular phase $\gamma_s = 0$ (the total charge of the pair is +1), m is the number of +− defect pairs with a charge $s = 1/2$ and an angular phase $\gamma_s = \pi/2$ (the total charge of the pair is +1), and finally n is the number of defect pairs with a charge $s = 1/2$ and $s = -1/2$, and an angular phase $\gamma_s = 0$ (the total charge of the pair is 0). The total topological charge of the $t\mathrm{P}^{ijk}_{lmn}$ defect is then

$$\chi(t\mathrm{P}^{ijk}_{lmn}) = i + j + l + m \tag{5}$$

Because the phase transitions only strictly happen in the thermodynamic limit, and thus no phase transition is expected in finite systems, we will refer to the obtained topological structures as the states of the considered system.

3 Simulation method

Langevin dynamics simulations were carried out for different systems of spherocylinders with packing fractions η changed between 0.3 and 0.9 by varying the aspect ratio of the rods in the range $4 \leq L/D \leq 24$ corresponding to the number of rods $700 < N < 4000$. During the Langevin displacement step the i-th particle position is changed from $\vec{R}_i$ to $\vec{R}_i^{\mathrm{new}} = \vec{R}_i + \delta\vec{R}_i$, where $\delta\vec{R}_i$ connects the old and new anchoring points of the i-th spherocylinder. Each positional displacement of the spherocylinder is also supplemented by orientational displacement move during which the orientation $\vec{n}_i$ of the rod is changed to $\vec{n}_i^{\mathrm{new}} = \vec{n}_i + \delta\vec{n}_i$ through the rotation of the rod around its center. At the new anchoring point the surface of the sphere is contacted by the center of the spherocylinder. Also, at this anchoring position the orientation $\vec{n}_i$ of the spherocylinder is always perpendicular to $\vec{R}_i^{\mathrm{new}}$. Both $\delta\vec{R}_i$ and $\delta\vec{n}_i$ are taken from Gaussian distributions. For the case of preordered orientation with angular constraint $\omega_i = \mathrm{const}$, the rotational Langevin step is replaced by the deterministic rotation of the rod. The new orientation $\vec{n}_i^{\mathrm{new}}$ in this case obeys the following three conditions,

$$\vec{n}_i^{\mathrm{new}} \cdot \vec{R}_i^{\mathrm{new}} = 0, \quad \vec{n}_i^{\mathrm{new}} \cdot \vec{e}_\theta = \cos\omega_i, \quad |\vec{n}_i^{\mathrm{new}}| = 1 \tag{6}$$

Here $\vec{e}_\theta = \vec{R}_i^{\mathrm{new}} \times [\vec{e}_z \times \vec{R}_i^{\mathrm{new}}]$. Eqn (6) guarantees a constant orientation of the rod relative to the longitudinal line of the sphere at the new anchoring position of the rod. The angular constraint, apparently, can be also managed by applying strong external forces orienting the rods in a given direction.

Once the particle i acquires a new position R_i^{new} and orientation $\vec{n}_i^{\mathrm{new}}$, the minimal distance $r_{ij}^{(m)}$ between it and its nearest neighbors is calculated using the method developed by Vega and Lago.[55] If an overlapping configuration with $r_{ij}^{(m)} < D$ is detected, then the particle i returned to its previous position $\vec{R}_i$ and orientation $\vec{n}_i$. In principle, it is possible to implement a more refined procedure proposed by Rebertus and Sando[56] for defining the impact time between the particles and calculating their new positions and orientations after each collision step. However this procedure slows down the simulation without any palpable gain in the precision of simulations.

Simulations were run in four consecutive steps. First, in the initialization step of simulations, a startup configuration with imprinted nematic order was created by anchoring the particles at random positions on the surface of sphere and imposing angular constraint on them. All anchored particles are allowed to make Langevin moves on the S_2. Second, in the equilibration step of simulations, the startup configurations with prescribed

ordering were equilibrated using Langevin dynamics. Third, in the relaxation step of simulations, we run additional Langevin simulations on the configurations with prescribed ordering and allow the rods to rotate freely around their radius-vectors. These free ordering simulations were run until a fully equilibrated state is reached. Fourth, in the production step of simulations, extended Langevin dynamics were run on the systems from the step 2 and step 3 simulations. During this final step of simulations necessary statistics on the density $\rho(\vec{r})$ and ordering parameter Q of spherocylinders were gathered with the aim to recognize defect structures and ordered configurations.

In the Langevin dynamics simulations the characteristic time τ for the spherocylinder center of mass to cover a distance D can be deduced from the typical kinetic energy of the spherocylinder, $k_BT \approx (D/\tau)^2$. Thus, $\tau \approx D\sqrt{m/(k_BT)}$. In carried simulations we use a time step h as a fraction of τ, $h = 10^{-3}\tau$. For high density systems $\eta \geq 0.8$ the time step was reduced to $h = 10^{-4}\tau$ for the better treating of the particle–particle overlappings. All preordered and relaxed configurations in the production phase of simulations were run for simulation times $10^4\tau$–$10^5\tau$.

4 Prescription of orientations

In the sequel, we consider three different systems with prescribed orientations shown in Fig. 2. In these systems, while the spherocylinders are anchored at random positions $\vec{R}_i$ on S_2, their orientation is constrained to prescribed directions.

4.1 Prescribed longitude ordering

In this case, the orientations $\vec{n}_i$ of all spherocylinders are kept parallel to the longitude lines on the sphere by fixing the orientation angle $\omega_i = 0$ for all rods. The corresponding morphology is shown in Fig. 2a. This configuration resembles an aligned liquid crystal system under a strong external field $\vec{E}_\theta$ directed along the polar angle vector $\vec{e}_\theta = \vec{R}_i \times [\vec{e}_z \times \vec{R}_i]$.

Under this field, the system develops a pair of full strength splay-like defects with the charges $s = 1$ and angular phases $\gamma_s = 0$ at the geometrical poles of the S_2. This configuration can be generated in experiments by putting electric dipoles on S_2 and placing oppositely charges particles on the poles of the S_2.

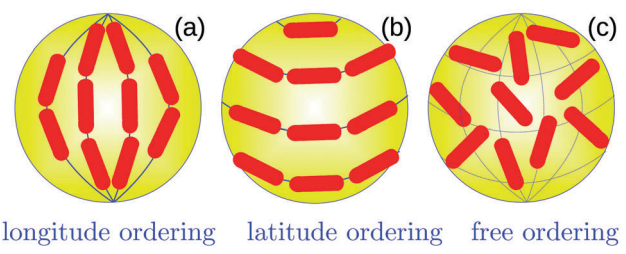

Fig. 2 Schematic pictures explaining the prescribed orientation fields: (a) a system with prescribed longitudinal orientation ("longitude ordering"), (b) a system with prescribed latitudinal orientation ("latitude ordering"), and (c) a relaxed system ("free ordering").

4.2 Prescribed latitude ordering

For prescribed latitude ordering, the orientations $\vec{n}_i$ of all spherocylinder are kept parallel to the latitude lines on the sphere at their anchoring point by fixing the orientation angle $\omega_i = \pi/2$ for all rods. The corresponding morphology is shown in Fig. 2b. This configuration resembles a liquid crystal system under a strong external field $\vec{E}_\varphi$ directed along the azimuthal angle vector $\vec{e}_\varphi = [\vec{e}_z \times \vec{R}_i]$. Under this field, the system develops a pair of bending-like defects with the charges $s = 1$ and angular phases $\gamma_s = \pi/2$ at the poles of the S_2. This configuration can be generated in experiments by considering magnetic dipoles on S_2 under the magnetic field of a current flowing through a wire connecting the poles of the sphere.

4.3 Free ordering

For the case of free ordering, the orientation vector $\vec{n}_i$ of the spherocylinder is allowed to freely rotate around its radius vectors $\vec{R}_i$. A corresponding system morphology is shown in Fig. 2c.

5 Protocol to obtain high density configurations

We develop a protocol for obtaining overlap-free initial configuration for high packing fractions. A continuous filling of the S_2 by a random insertion of spherocylinders has an acceptable success rate until the packing fraction $\eta \approx 0.45$ is reached. This packing value slightly depends on the aspect ratio L/D of spherocylinders. Above this threshold the jamming of rods on S_2 increases the rejection rate of the attempted insertions, and, as a result of it, the random insertion method eventually stalls. Overcoming this barrier is a complicated problem, and one of the possible solutions to it is based on artificially generating a smectic crystal at the desired packing fraction, and then melting it in the simulations. This top down approach lacks the crucial information about the onset of the smectic phase formation from the nematic ordering.

We propose a new bottom up method consisting of two consecutive stages which successfully resolves the jamming issue observed for longitude and latitude orderings. In the first stage of simulations we couple the particle insertion with the Langevin dynamics displacement for all particles placed on S_2. In addition to the Langevin displacement of spherocylinders, we also implement Monte-Carlo type long distance moves on S_2: for the randomly chosen particle j an attempt is made to relocate it into other spots on S_2. Both the Langevin displacements and occasional Monte-Carlo moves tremendously increase the chances to reach the packing fraction $\eta \approx 0.7$, which slightly depends on the aspect ratio L/D.

To go beyond this threshold, we implement another helpful procedure in the second stage of simulations. We start to insert thinner particles with reduced diameter $D_i = 0.85D$, hence with larger aspect ratio L/D_i, and then, during the following Langevin and Monte-Carlo-type displacements in the initialization step, we calculate the minimum separation distance Δr between the

thinner particle and its neighbors. The particle diameter is then increased from D_i to $D_i + \Delta r/2$ during the next step in the initialization phase. This procedure is repeated until D_i reaches D. An implementation of this procedure makes it possible to reach higher densities as $\eta = 0.85$ in the longitude preordered systems, and $\eta = 0.9$ in the latitude preordered systems in the initialization startup part of simulations. We note that our bottom up approach based on the above mentioned two stages completely differ from previous studies for achieving a smectic phase at high densities. Whereas in previous studies the smectic phase was formed from the melting of the crystalline phase, our approach presents a more natural way for generating high density smectics with characteristic thermal fluctuation imprints in it. Also, our approach differs from the one used in ref. 28 where only short spherocylinders $L/D \leq 1$ were considered for getting close packed and random structures on spherical surfaces without any focus on the nematic-to-smectic transition.

It should be noted that there is an alternative, and seemingly more natural method for generating startup configurations with higher density. In this method random particle positions are generated on an oversized sphere. Then the sphere size is slowly decreased until the required density is reached. Our test simulations showed that the slowly decreasing sphere method has its own limitations: around the density $\eta \approx 0.7$ the method becomes extremely slow because of the increased aggregation of the moving particles into smectic-like clusters. These clusters prevent further decreasing of the sphere size. Therefore, for reaching higher densities $\eta = 0.9$ the only available option is still the random insertion of thinner particles described above.

6 Density modulations in smectics

In this section we will focus on the density modulations in smectic phases. The layering of particles in the smectic phase on the spherical surface of radius R is characterized by the wavevector $q = 2\pi/d_\theta$, where $d_\theta = R\theta_0$. We consider a smectic phase with longitudinal ordering when the normal to the smectic layer is parallel to the unit vector $\vec{e}_\theta$ tangential to the meridian, see the schematic picture shown in Fig. 3. The particle density can be developed in a Fourier series

$$\rho(\varphi,\theta) = \rho_0 + \rho_1 \cos[q(R\theta + u_\theta(\varphi))] + \cdots \quad (7)$$

where $u_\theta(\varphi)$ is the layer displacement field along the layer normal from the equilibrium position $\theta = n\theta_0$ of the n-th layer. This displacement field depends on the in-layer position φ because of the Landau–Peierls fluctuations which become stronger as the lateral size of the smectic layer $L_\varphi = R\varphi$, or equivalently, the the opening angle φ of the layer becomes larger. The mean square of these fluctuations in 3D smectic phases[57]

$$\langle u^2(r)\rangle_{3D} \propto \frac{k_B T}{\sqrt{C}} \ln\left(\frac{L_{Sm}}{d}\right) \quad (8)$$

diverges with the smectic layer lateral size L_{Sm}, resulting in the loss of the smectic ordering when $\sqrt{\langle u^2\rangle} \approx d_\theta$. In eqn (8) C is the elastic modulus of the layers.

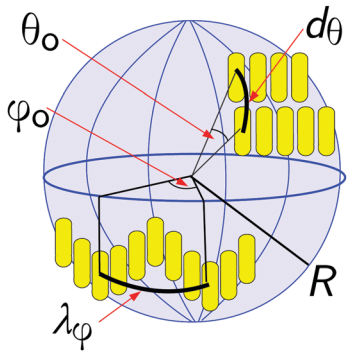

Fig. 3 A schematic picture explaining the spacing $d_\theta = R\theta_0$ between adjacent layers, see the north hemisphere, and the modulation wavelength $\lambda_\varphi = R\varphi_0$, see the south hemisphere, in the smectic phase with longitudinal ordering.

In some particular cases the Landau–Peierls instability, instead of destroying the smectic ordering, might generate periodic modulations to the displacement field $u(\vec{r})$. For example, recently Tavarone *et al.*[58] detected such modulations for a bow shaped particles on a flat surface. Assuming that similar density oscillations might also develop in smectic layers generated on spherical surfaces, we describe them as $u_\theta(\varphi) = u_\theta \cos(\varkappa\varphi)$, where $\varkappa = 2\pi/\lambda_\varphi$ and $\lambda_\varphi = R\varphi_0$ are the wavevector and wavelength of these oscillations along the azimuthal angle φ, respectively, and u_θ is the amplitude of these oscillations along the polar angle θ. Consequently, the following smectic order parameter Λ_{Sm} can be introduced to quantify the layer modulations,

$$\Lambda_{Sm}(q,\varkappa) = \left\langle \frac{1}{N}\left|\sum_{j=1}^{N} e^{i\vec{q}\vec{e}_\theta R\theta_j} e^{i\vec{\varkappa}\vec{e}_\varphi R\varphi_j}\right|\right\rangle \quad (9)$$

Here $\vec{e}_\theta$ and $\vec{e}_\varphi$ are the unit vectors tangential to longitude and latitude lines at the anchoring position for the j-th rod. For larger wavelengths $\lambda_\varphi \geq 2\pi R$, eqn (9) describes ordinary smectic order parameter $\Lambda_{Sm}(q)$ without in-layer modulations.[59] We calculate $\Lambda_{Sm}(q,\varkappa)$ for different values of λ_φ and directions $\vec{h}$ and regard the maximal value of the Λ_{Sm} as the smectic order parameter for the considered system.[58] A configuration with $\Lambda_{Sm} \geq 0.5$ is regarded as a smectic phase, otherwise it is assumed to be a nematic phase. The threshold value 0.5 corresponds to the local fluctuations in the particle position in each layer not exceeding 15% of the layer–layer distance d_θ.

In the following we use the diameter of the spherocylinder D as a unit for distance and thus the aspect ratio will be denoted as L. Also, the caps and central area of the S_2 will be referred as the poles and equator of the sphere, respectively.

7 Simulation results

7.1 Rods with prescribed longitude ordering

The state diagram of the system of rods with prescribed longitude ordering is shown in Fig. 4 in the variables L and η. Two different smectic states develop from the nematic startup configurations: the position of the nematic–smectic transition

line was defined from the smectic order parameter Λ_{Sm} from eqn (9).

In Fig. 5 the normalized polar density of particles $\rho(\theta)/\rho_0$ is plotted for $L = 6$ and three packing fractions $\eta = 0.6$, 0.7, and 0.8. Here $\rho_0 = N/(4\pi R^2)$ is the average density of rods on the S_2. For $\eta = 0.6$ and 0.7, which are shown as a nematic state in Fig. 4, there are regular density fluctuations at the poles of S_2. This means that the smectic layering first forms at the poles, and then gradually develops towards the equator of the sphere. For $\eta = 0.8$ the particle density fluctuations are strongly sinusoidal

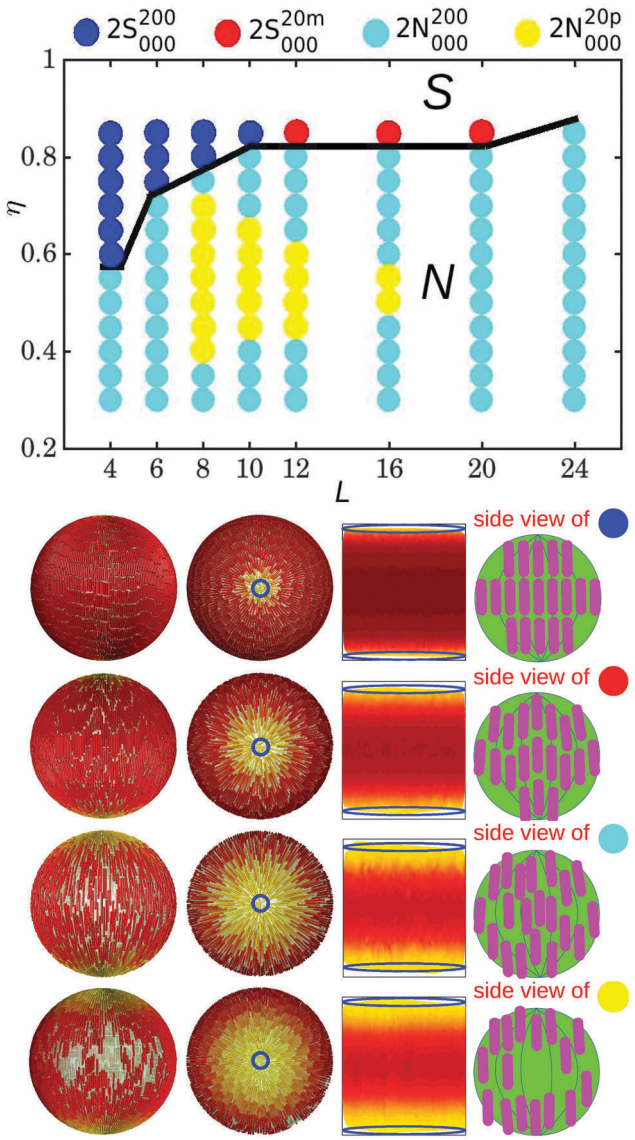

Fig. 4 State diagram of the system of rods with prescribed longitude ordering. The black solid line indicates the nematic (N) to smectic (S) transition. Different defect structures are identified by separate colors and codes. The codes for the defects are given at the top of the diagram. Representative side-view and top-view snapshots for each defect structure are provided below the state diagram together with 2D ordering map for the eigenvalues λ_+ of the local orientation parameter Q_i^j given by eqn (10) and a schematic picture explaining the morphology of the particle distribution on the spherical surface.

which is the fingerprint of the smectic state. The distance between the adjacent peaks of $\rho(\theta)$ in this case defines the inter-layer distance d_θ in the smectic ordering.

From the Fig. 5 it is seen than $\rho(\theta)$ is zero at $\theta = 0$. This observation has a simple explanation. The density $\rho(\theta)$ was calculated for 90 grid points with the grid width $\Delta\theta = \pi/90$. Thus, $\rho(0)$ corresponds to the number of particles inside a conical segment centered at the north pole $\theta = 0$ with a cone opening $\Delta\theta$. For $\eta = 0.8$ and $L = 6$ the surface area of this polar segment appears to be twice smaller than the average surface area $1/\rho_0$ per particle on the S_2. As a consequence, the polar segment has an occupancy rate of less than 50%. Therefore, it is just a coincidence that for the configurations used in Fig. 5 the polar segment was empty from rods, $\rho(0) = 0$.

In Fig. 4, the N–S transition line starts at $\eta = 0.55$ for the smaller rods $L = 4$, and reaches $\eta = 0.85$ for the longer rods $L = 24$. This upturn tendency of the transition line can be explained by the increase of the curvature effect at larger L/R ratios. When L/R is big, the discrepancy between the orientations of neighboring particles increases, which makes the clustering of particles into smectic layers less effective. It should be noted that the N–S transition observed here is completely different from the previous studies, where the N–S transition was obtained from the melting of the smectic state that was artificially created by stacking of hexagonal ordered layers.[10] In our study the smectic state is formed consistently in a dense nematic state due to the particle–particle hard-core interactions.

The two types of smectic states in Fig. 4 are tagged as blue dots for $L \leq 10$, and red dots for $L \geq 12$. The blue dot smectic state, coded as $2S_{000}^{200}$, has 2 splay-like defects at the poles with charges $s = 1$ and angular phases $\gamma_s = 0$. The snapshot pictures, the orientation order parameter map, and a schematic picture explaining the morphology of the particle distribution for this state are shown at the bottom of Fig. 4 in the figure line 1 for

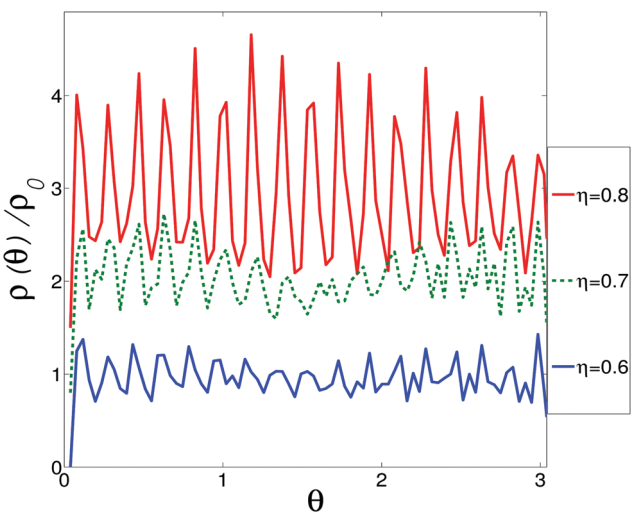

Fig. 5 Normalized polar density $\rho(\theta)/\rho_0$ of particles for $L = 6$ from Fig. 4 for three packing fractions η. The nematic–smectic transition appear between $\eta = 0.7$ (shifted upward by one unit) and $\eta = 0.8$ (shifted upward by two units).

the simulation run for $L = 6$ and $\eta = 0.85$. The orientation order parameter map was plotted for the eigenvalues $\lambda_+(\varphi_i,\theta_i)$ of the local orientation order tensor Q_i^i with elements

$$Q^i_{\alpha\beta} = \frac{1}{2N_i}\left(\sum_{j=1}^{N_i} 3n_{j\alpha}n_{j\beta} - \delta_{\alpha\beta}\right) \quad (10)$$

where N_i is the number of neighboring rods around the i-th rod with their anchoring points laying inside a spherical sector with a cone opening angle $\pi/6$, α, $\beta = x, y, z$, $\delta_{\alpha\beta}$ is the Kronecker delta, and $n_{i\alpha}$ and $n_{i,\beta}$ are the components of the molecular axis of the i-th rod. In the 2D order map the x-axis represents the azimuthal angle φ and changes from 0 to 2π, and the y-axis represents the polar angle θ and changes from 0 to π. For uniaxial nematics $\lambda_+ > 0$ and the corresponding eigenvector $\vec{n}$ gives the orientation of the nematic director field. The colors from blue to red in the orientation order parameter map in the figure lines of Fig. 4 correspond to the change of $\lambda_+(\varphi_i,\theta_i)$ from 0 to 1.

The defect positions at the poles are marked as a hollow blue circle in the top view snapshot picture and as an oval blue line in the orientation order parameter map. The yellow color at the defect positions at the poles in the orientation order map in the figure line 1 corresponds to less than 50% of orientational ordering of the rods, and the dark red color at the equator of the map corresponds to more than 90% of orientational ordering of the rods. The same coloring scheme was also used for the particles in the snapshot pictures.

It is interesting to note that the coloring of the rods in the snapshots in Fig. 4 correlates with the ratio K_1/K_3 of the Frank elastic constants. The Frank-Oseen elastic energy density depends on the deformation of the local director field $\vec{n}(\vec{r})$ as[27]

$$f_{el} = \frac{1}{2}K_1(\vec{\nabla}\cdot\vec{n})^2 + \frac{1}{2}K_3(\vec{n}\times(\vec{\nabla}\times\vec{n}))^2 \quad (11)$$

where K_1 and K_3 refer to the splay and bending modulii, respectively. The splay-like structure of the defects in the figure line 1 in Fig. 4 means that in the vicinity of the poles $K_1 \ll K_3$. Hence, the yellow region on the S_2 corresponds to the smaller values of K_1/K_3. Away from the poles and towards the equator the rods become more parallel to each other, and the splay energy vanishes. Hence, the dark red region on the S_2 corresponds to the higher values of K_1/K_3. The exact values of the Frank constants can be calculated using the Fourier transformation of the Q_i^i tensor (see eqn (10)).[59–61]

The red dot smectic state, coded as $2S_{000}^{20m}$, has also two splay-like defects with the charges $s = 1$ and angular phases $\gamma_s = 0$ at the poles. However, away from the poles the smectic state has azimuthal modulations with "broken egg-shell" like patterns. Representative snapshots and orientation ordering map are given in the figure line 2 for the simulation run for $L = 12$ and $\eta = 0.85$. For better recognition of the zig-zag like structure of this defect, we emphasize the layer modulations by showing the layer boundaries as yellow lines in Fig. 6. The formation of

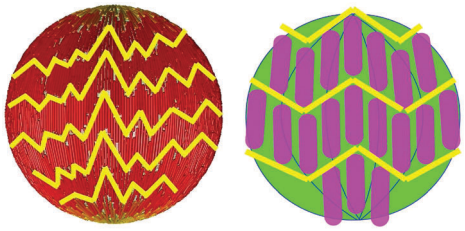

Fig. 6 The "broken egg-shell" like modulated smectic state from Fig. 4 line 2. Left picture: A snapshot from simulations. Right picture: A schematic picture. The yellow lines are a guide for the eye and show the boundaries of the layers.

the broken-egg like structure can be examined by the calculation of the zig-zag order parameter

$$\Psi(u_\alpha,\lambda_\beta) = \frac{1}{N_j}\sum_{j}^{N_j}\cos\left[\frac{2\pi}{d_\alpha}\left(R\alpha_j + u_\alpha\sin\left(\frac{2\pi}{\lambda_\beta}R\beta_j\right)\right)\right] \quad (12)$$

where u_α is the amplitude of the modulations, λ_β is the wavelength of the modulations, α and β are the polar and azimuthal angles of the rods in a spherical system of coordinates with $\vec{z}$-axis oriented in arbitrarily chosen direction. The values of the fitting parameters u_α and λ_β at which $\Psi \geq 0.5$ are considered as the amplitude and wavelength of the zig-zag structure, respectively. For the broken-egg structure oriented parallel to the equator, like the situation observed in Fig. 6, the angles α and β in eqn (12) should be replaced by the angles θ and φ respectively. For the case when the broken-egg structure is oriented parallel to the meridian lines of the sphere, the angles α and β in eqn (12) should be replaced by the angles φ and θ respectively. For the line 2 in Fig. 4 the order parameter was found to be $\Psi = 0.56$ at the equator area for the best fits $u_\theta \approx L$ and $\lambda_\varphi \approx 1.5L$. We believe that the origin of these modulations is the interplay between the Landau–Peierls instability discussed in Section 6, eqn (8), and the curvature effect at large L/R ratios. For getting a better understanding of these periodic layer undulations, additional simulations on the toroid surface which has total charge $\chi = 0$ should be run. In ref. 58 similar layer modulations were detected for the 2D planar system with bow shaped particles.

Below the N–S transition line in Fig. 4, there are two types of the nematic states, coded as $2N_{000}^{200}$ and $2N_{000}^{20p}$ and tagged as cyan and yellow dots, respectively. Both these states have splay-like defects at the poles with charges $s = 1$ and angular phases $\gamma_s = 0$. Representative snapshots and orientation order maps for these states are shown in figure lines 3 and 4 of Fig. 4 for the simulation runs $L = 16$ and $\eta = 0.7$, and $L = 8$ and $\eta = 0.75$ respectively. The main difference between these two structures is the existence of a particle-free bald patches in the $2N_{000}^{20p}$ structure (the index 'p' here means a 'patch') at the equator of S_2. The following two factors contribute to the emergence of bald patches at the equator of S_2. First, the distribution of rods on S_2 in the nematics corresponding to the yellow dotted area in Fig. 4 is inhomogeneous: the particle density is higher at the poles compared to their density at the equator of S_2. This inhomogeneity results from the competition between the excluded volume F_η and

orientation F_α parts of the free energy (see Appendix A). Since the particles are prohibited to rotate freely, their excluded volume free energy F_η has no dependence on the ordering degree parameter α and is constant on the S_2. The ordering degree parameter α is 1 at the equator, and zero at the poles. Therefore F_α in this area is smaller than its value at the equator. This makes the poles energetically more favorable place for the particles.

Second, the higher particle density at the poles generates smectic ordering in that area. For example, as seen from the snapshots of the state $2N_{000}^{20p}$ in the figure line 4 of Fig. 4, the local packing fraction reaches 0.8 at the poles where a smectic layering is observed. As a consequence, a transition region appears between the low-density nematic phase at the equator and the high-density smectic phase at the poles. This transition region has a biphasic nematic–smectic structure. The width of this coexistence region D_{coex} depends on the curvature parameter L/R, the aspect ratio L/R, and the density η of the rods. If $D_{\mathrm{coex}} > \pi R$, which is the case for the figure line 4 of Fig. 4, then the transition regions belonging to the north and south hemispheres overlap at the equator. In other words, the pure nematic phase at the equator will be annihilated. Though the biphasic transition region has no impact on the continuous transition in the polar density of rods, the local distribution of particles inside the biphasic region will not be homogeneous.

The bald patches can be used in functionalization applications. For example, their functionalization with target molecules or chemical linkers (see discussion in ref. 52) will provide the spheres with directional interactions. As a result of this, the spheres will be able to form 2D free standing sheets which can be used to create other single layer structures such as graphene tubes. Similar structures were found in the system of particles accompanying Saturn-ring defects.[62] Such defects form on the particle surface placed in the nematic liquid: upon nematic ordering, a closed disclination loop binds more than two particles to form a sheetlike dynamically arrested structure.

7.2 Rods with prescribed latitude ordering

The state diagram of the system of rods with prescribed latitude ordering is shown in Fig. 7. Five possible states are detected with the three of them being in a smectic state and the two of them being in a nematic state. The N–S transition line here was also detected by calculating the smectic order parameter Λ_{Sm} from eqn (9). The initial downturn of the transition line at low L, between $L = 4$ and $L = 8$, is induced by the caging effect of longer spherocylinders. The caging of the particle by its nearest neighbors can be defined as the ratio of the cage size to the particle length, $\Gamma = \sqrt{\delta A}\Big/L$. Here $\delta A = 4\pi R^2/N$ is the area available per particle on the S_2. Comparing two states with $L_1 = 4$ and $L_2 = 8$ at $\eta = 0.5$ in Fig. 7, and assuming that $N_1 \approx 2N_2$, we get $\Gamma_2 = 2R\sqrt{\pi/N_2} \approx \sqrt{2}\Gamma_1$. In other words, the caging effect tends to be stronger in systems with longer particles. In an analogy with the N–S transition associated with the strengthening of the caging effect when η increases at the fixed L, it is reasonable to expect a similar N–S transition for longer rods with higher

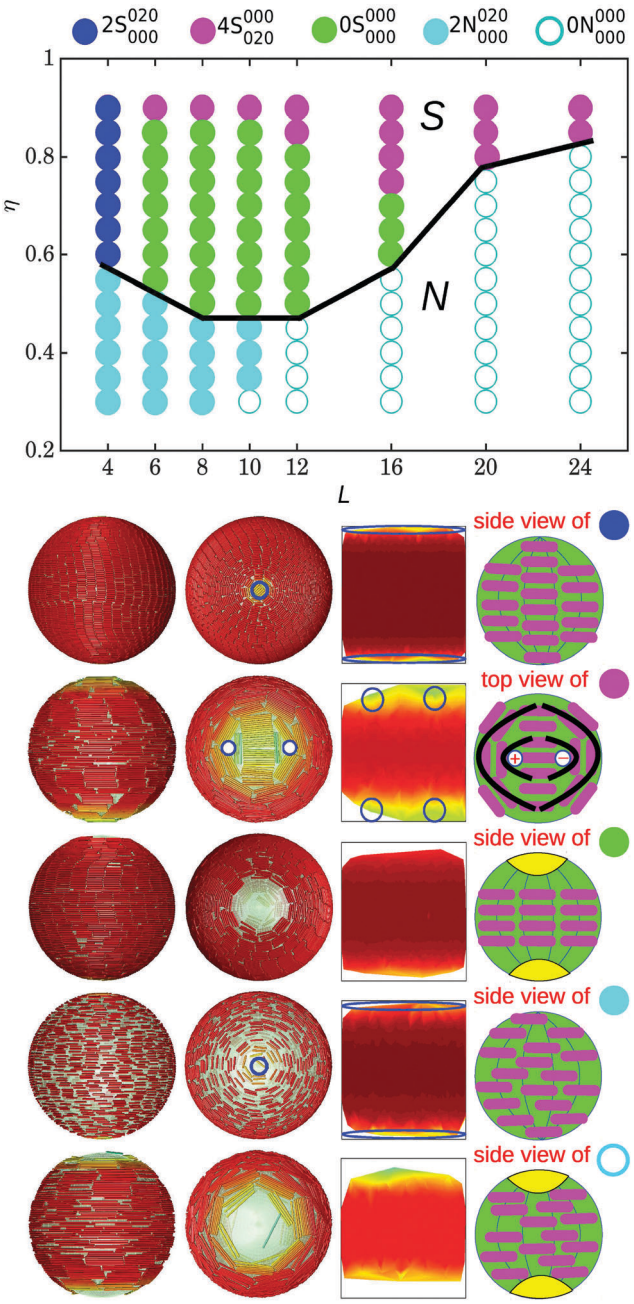

Fig. 7 Same as in Fig. 4, but now for latitude ordering. Different defect structures are identified by separate colors and codes. The codes for the defects are given at the top of the diagram.

caging parameter Γ at fixed η. Note that for larger L the curvature effect L/R becomes stronger enough to destroy the smectic layering at intermediate packing fractions η. This explains the upturn of the transition line at $L \geq 12$ in Fig. 7.

All the states in Fig. 7 have bending-like configurations with high bending energy near the defects (at the poles), and low bending energy at the equator of S_2. This inhomogeneous distribution of the bending energy, or the Frank constant K_3 (see eqn (11)), will definitely make the equator more energetically favorable place for the particles. Consequently, the orientational coloring used in the snapshots in Fig. 7 correlates with

the ratio of the Frank constants, K_1/K_3. The yellow area at the poles corresponds to the higher values of K_1/K_3, whereas the dark red region at the equator corresponds to the smaller values of K_1/K_3. The probing of the states in Fig. 7 by eqn (12) showed that $\Psi < 0.5$ for all possible configurations of α and β. Therefore there is no pronounced broken egg-shell like structure in Fig. 7 for systems with prescribed latitude ordering.

The first smectic state, coded as $2S^{020}_{000}$, meaning a state with two full defects with charges $s = 1$ and angular phases $\gamma_s = \pi/2$ at the poles, is tagged as blue dots in Fig. 7. This state appears only at the lowest particle length $L = 4$. Representative pictures including snapshots, orientation order map and a schematic picture are shown in the figure line 1 below the state diagram for the simulation run for $L = 4$ and $\eta = 0.9$.

The second smectic state, coded as $4S^{000}_{200}$, meaning a structure with four half-strength defects with $s = 1$ and $\gamma_s = \pi/2$ near the poles, is tagged as magenta dots in Fig. 7. Representative snapshots are shown in the figure line 2 below the state diagram for the simulation run for $L = 16$ and $\eta = 0.8$. As seen from the schematic picture for this state, the pair of defects form a +− binding at the poles, which is highlighted by the black lines. This binding is the result of the splitting of the $s = 1$ and $\gamma_s = \pi/2$ full strength defect shown in Fig. 11 in Appendix B. In ref. 63 it is shown that such +− binding is curvature-driven and the interaction between the defects depend on their separation. At very low and large distances the two defects repel each-other, whereas at intermediate distances they are attracted to each-other.

The third smectic state, coded as $0S^{000}_{000}$, meaning a structure without any defects, is tagged as green dots in Fig. 7. Representative snapshots are shown in the figure line 3 below the state diagram for the simulation run for $L = 8$ and $\eta = 0.85$. Because of the high bending energy near the poles, the particles mostly accumulate at the equator leaving the poles empty in the systems with intermediate packing fractions η. This type of smectic morphology has never been reported in the literature. A potential application of this state, after the functionalization of its poles with target molecules, might be the formation of string-like wires of the colloidal spheres.

The nematic state below the N–S line in Fig. 7, splits into two different classes. The first class, coded as $2N^{020}_{000}$, meaning a structure with two full defects with $s = 1$ and $\gamma_s = \pi/2$, is tagged as cyan dots. Representative pictures for this low curvature L/R and low η state are given in the figure line 4 below the state diagram for the simulation run $L = 6$ and $\eta = 0.45$. The second class, coded as $0N^{000}_{000}$, meaning a structure with empty polar caps and no defects, is tagged as open cyan circles. Representative pictures for this state are given in the figure line 5 below the state diagram for the simulation run $L = 20$ and $\eta = 0.7$. This state resembles the smectic state with empty poles $0S^{000}_{000}$, and appear in systems with large curvature parameter L/R. This state also can be used in colloidal applications to generate 1D wires of colloidal spheres.

An interesting observation happens when η increases from 0.3 to 0.9 for the fixed length $L = 10$. First, the nematic system with empty poles converts into a nematic state with two full defects at the poles. Second, this nematic state with polar defects transfers into a smectic state with empty poles. Third, the empty pole smectic evolves into a smectic state with +− binding defects at the poles. These three-step N–S transition is different from the single-step N–S transition on the flat surfaces.

7.3 Rods with free ordering on S_2

When the orientational ordering constraint for the rods is released, the systems with prescribed longitude and latitude orderings will relax into new configurations. The thermalization of the preordered morphologies will redistribute their splay and bending energies evenly on S_2. The resulting states are shown in Fig. 8. Representative snapshot and schematic pictures for the observed morphologies are gathered in Fig. 9.

According to Fig. 8, there is no N–S transition in relaxed and freely rotated systems. This fact is associated with the existence of the main topologically invariant half-strength defects and the development of extra dipolar structures consisting of positive and negative half-strength defects. The structural diffusion and even presence of these disclinations will destroy any smectic ordering on the S_2. Obviously, the finite size effects also contribute to this picture. To minimize the finite size effects larger systems with more particles on the surface of bigger spheres with the same curvature parameter L/R are needed.

As seen from Fig. 8, there is a universal threshold value $\eta = 0.8$ below which the relaxed states have no memory about their initial state. All relaxed states are isotropic for $L \leq 10$, this state is noted as I and is tagged as an open magenta circle in the state diagram. Representative pictures for the state I are shown in Fig. 9 on line 1 for $L = 8$ and $\eta = 0.8$. There is a well-defined cluster size of the smectic domains in high density isotropic phases. The dependence of the cluster size on the system parameters η and L can be deduced from the correlations in Q^i_l.

For $L > 10$ in both state diagrams in Fig. 8, two different nematic states are observed. The first nematic state is close to the threshold value $\eta = 0.8$ and is coded as $4N^{004}_{000}$, meaning that there are 4 half-strength defects with $s = 1/2$ and $\gamma_s = 0$. The upper row index '4' in the code indicates that all the four half-strength defects are freely moving disclinations. This state is tagged as a red circle with a red dot in it. Representative pictures for this structure are shown in Fig. 9 on line 2 for $L = 16$ and $\eta = 0.8$. During the simulation runs the defects occasionally form structures resembling the nodes of the tetrahedron. The morphology of the particle orientation between the neighboring defects resembles a part of the baseball like structure, as illustrated in the schematic picture for the $4N^{004}_{000}$ state in the figure line 2.

The second nematic state is close to the nematic–isotropic (N–I) transition line and is coded as $8N^{004}_{002}$, meaning that it has 8 half-strength defects, with 4 of them being positive with $s = 1/2$ and $\gamma_s = 0$, and other 4 of them forming two dipolar structures. This state is tagged as a red circle with a dark green dot in it. Representative pictures for $8N^{004}_{002}$ are shown in Fig. 9 on line 3 for $L = 16$ and $\eta = 0.6$. Each dipolar structure has a positive and negative half-strength defects with charges $s = 1/2$

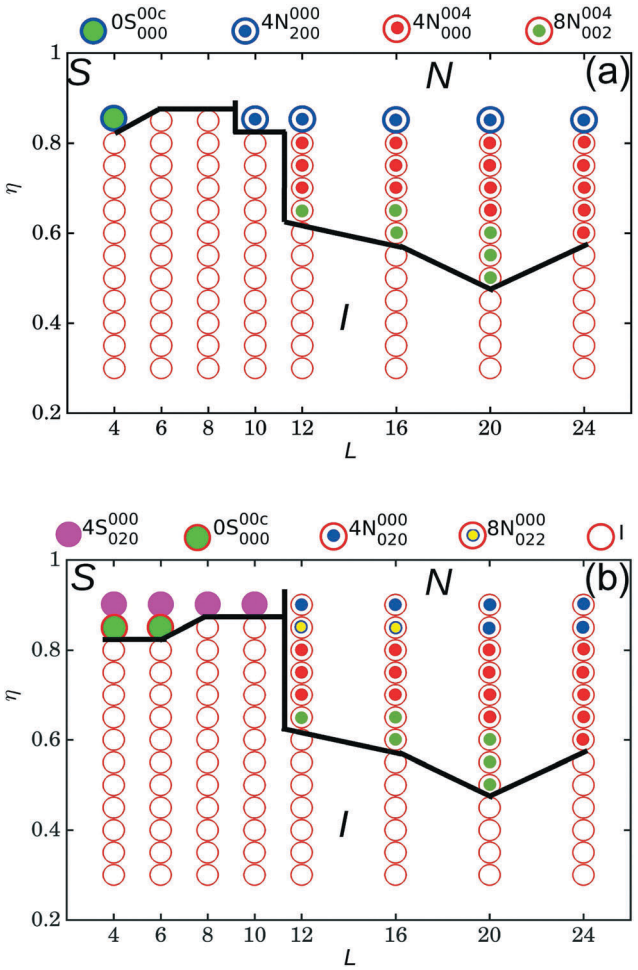

Fig. 8 The state diagram of a system relaxed from rods with prescribed longitude ordering (a), and from rods with prescribed latitude ordering (b). Different defect structures are identified by separate colors and codes. The codes for the defects are given at the top of the diagram. Snapshots and more details are given in Fig. 9.

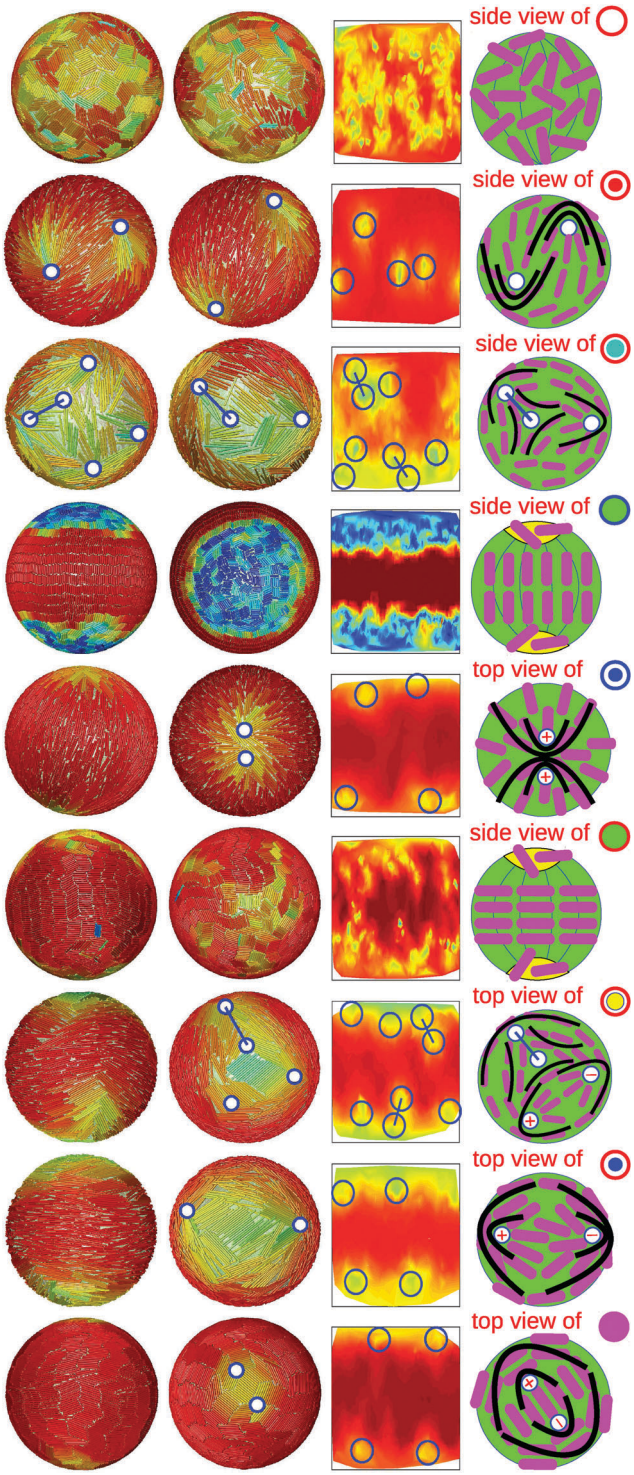

Fig. 9 Representative pictures for the defect structures from Fig. 8. Same as in Fig. 4 but now for free ordering. From top to bottom: I, $4N^{004}_{000}$, $8N^{004}_{002}$, $0S^{00c}_{000}$, $4N^{000}_{200}$, $4S^{00c}_{000}$, $8N^{000}_{022}$, $4N^{000}_{020}$, $4S^{000}_{020}$.

and $s = -1/2$ and angular phases $\gamma_s = 0$, thus its total charge is zero. From the shape of the director field $\vec{n}$ lines around the dipolar structure, shown as black lines in the schematic picture for this defect structure, it can be contemplated that the dipolar structure has a cap near its positive charge area, and two legs near its negative charge area. Like the state $4N^{004}_{000}$, here also the defects change their position on S_2 through structural diffusion during the simulation runs. However, the positive and negative defects of the dipolar structure are always closely associated with each other, which is shown as a blue line in the representative pictures for this state. Also, it was detected that one of the positive half-strength defects has a close association with the leg part of the dipolar structure, or more clearly, with the negative charge of the dipolar structure. This association makes it possible for the dipolar structure to structurally diffuse by accepting the positive half-strength defect as a new cap and releasing its old cap as a free positive half-strength defect. In other words, the reassembling of the half-strength defect – dipolar structure configuration into a dipolar structure – half-strength defect configuration adds dynamics to the dipolar and defect structures. This mechanism can be assumed as the macroscopic realization of the defect motion in crystalline solids.[64–66]

Above the threshold value $\eta = 0.8$, the relaxed system keeps a partial memory about its initial configuration. For $\eta = 0.85$ from

the 2 types of smectic states in Fig. 4 for the system with prescribed longitude ordering only the state $2S_{000}^{200}$ for $L = 4$ survives, though partially. The new relaxed state is now coded as $0S_{000}^{00c}$ and tagged as a blue circle with a green interior in Fig. 8a. In this state the initial smectic ordering is reduced to the equator, whereas the poles have isotropic states (the index 'c' in the code means an iso-cap). Representative pictures for this state are shown in Fig. 9 on line 4 for $L = 4$ and $\eta = 0.85$. As it was mentioned before in Section 7.1, the poles of the initial state $2S_{000}^{200}$ has higher splay deformation energy compared to the equator, thus it was the prime candidate to decrease its elastic energy when relaxed. Accordingly, the equator with lesser elastic energy in the initial state was able to survive the relaxation process. The width of the equatorial band strongly depends on L: as L increases, the curvature effects become stronger meaning higher values for the single Frank constant K. As a result of it, the isotropic phase at the poles of the relaxed system will propagate deeper into the equator of S_2 and thus the band size will decrease.

The other smectic states at $\eta = 0.85$ in Fig. 4, namely the states $2S_{000}^{200}$ and $2S_{000}^{00m}$, when relaxed, convert into the I state for $L = 6$ and $L = 8$, and into a new nematic state $4N_{200}^{000}$ for $L \geq 10$. In this new state, tagged as a blue circle with a blue dot in it in Fig. 8, there are 4 half-strength defects with $s = 1/2$ and $\gamma_s = 0$, and the defects are paired into the ++ binding at the poles. Representative pictures for $4N_{200}^{000}$ are shown in Fig. 9 on line 5 for $L = 12$ and $\eta = 0.85$. In this type of binding, discussed in Appendix B, the defects strongly repel each-other, however, because of the extremely high density of the overall structure, the defects cannot diffuse away from each-other. Only at smaller packing fractions, see the line 3 in Fig. 9, the ++ binding dissolves into a pair of free half-strength defects.

The relaxation of the initially latitude oriented system at the highest packing fractions $\eta = 0.85$ and $\eta = 0.9$ appears to be even more complex. From the initial smectic states $2S_{000}^{020}$ and $4S_{020}^{000}$ in Fig. 4 at $\eta = 0.85$ only the two low aspect ratios $L = 4$ and $L = 6$ smectics partially survive the relaxation procedure. Again, similar to the relaxed state $0S_{000}^{00c}$ in Fig. 8a, in the new state the equator has smectic morphology whereas the poles become isotropic. In this case, however, it is the high bending elastic energy in the initial configuration which destroys the defects in the cap during the relaxation process. The obtained new state is coded as $0S_{000}^{00c}$ and tagged as a red circle with a green interior. Representative pictures for this state are shown in Fig. 9 on line 6 for $L = 6$ and $\eta = 0.85$. The only difference between this state and the other similar state shown on line 4 is the orientation of the smectic state at the equator. In the former state the orientation of the rods was perpendicular to the cap boundary, whereas in the latter state the rods are parallel to the cap boundary.

All the other smectic states at $\eta = 0.85$ for $L \geq 8$ for the initially latitude oriented system completely loss their initial morphology during the relaxation process. For the $L = 12$ and $L = 16$ cases the $4S_{020}^{000}$ smectic state with +− binding at the poles relaxes to the nematic state $8N_{022}^{000}$. This state is tagged as a red circle with a yellow dot in it, and has 8 half-strength defects from which the 4 half-strength defects with $s = 1/2$ and $\gamma_s = 0$ form a +− binding in the cap areas of the S_2. The other 4 defects form 2 dipolar structures also in the cap area and near the +− bound half-strength defects. Representative pictures for this state are shown in Fig. 9 on line 7 for $L = 16$ and $\eta = 0.85$. This structure can be viewed as a transitional structure which, at the low packing fractions η, transfers into the $4N_{000}^{004}$ state through the fusion of the negative charge of the dipolar structure with one of the charges of the the +− binding. Such fusion results in the dissolution of the dipolar structure and the +− binding, and the formation of a pair of separate half-strength defects with positive charges $s = 1/2$.

The other two smectics $4S_{020}^{000}$ in Fig. 7 for the initially latitude preordered system at $\eta = 0.85$ for $L = 20$ and $L = 24$, relax into the nematic state $4N_{020}^{000}$ with the same 4 half-strength defects with $s = 1/2$ and $\gamma_s = 0$ which group into +− bindings at the poles In other words, the relaxation only affects the smectic layering of the initial state, replacing it by the nematic ordering. This state is tagged as a red circle with a blue dot in it, and the representative pictures are shown in Fig. 9 on line 8 for $L = 20$ and $\eta = 0.9$.

Finally, the smectic state $4S_{020}^{000}$ at the highest packing fraction $\eta = 0.9$ in the latitude preordered system basically keeps its initial morphology for $L \leq 10$ during the relaxation process. In these low curvature and high η systems, the initial smectic layering can be viewed as a morphology with frozen structure. This state, similar to the state $4S_{020}^{000}$ in Fig. 7, is also tagged as magenta dots and representative pictures are shown in Fig. 9 on line 9 for $L = 10$ and $\eta = 0.9$. For $L > 10$ the strong curvature effects destroy the smectic layering during the relaxation process. The resulting relaxed system appears to be in the nematic state $4N_{020}^{000}$. The defects stay the same, only the smectic layering is gone during the relaxation process.

The probing of the states in Fig. 9 by eqn (12) showed that $\Psi < 0.25$ for all possible configurations of α and β, a clear indication of the absence of zig-zag like structures in relaxed systems.

An interesting observation occurs in Fig. 8a, when for the fixed $L = 16$ the packing fraction η is decreased from 0.85 to 0.5 for the relaxed nematic state $4N_{200}^{000}$. This state has four half-strength defects with ++ bindings at the poles. First, as the density is decreased, the defects start to distance from each other because of their mutual repulsion. They occupy random positions on S_2 and form a baseball like structure with their neighbors. Second, near the N–I transition line additional defects with dipolar structures appear, which interact with the 4 half-strength defects and facilitate their structural diffusion across the S_2. Third, the highly mobile defects at low densities disturb, and eventually damage the nematic state pushing the system into the isotropic state.

If the starting position is chosen to be the highest density state $4N_{020}^{000}$ at $\eta = 0.9$ for the fixed $L = 16$, see Fig. 8b, then the above step one, namely the separation of the defects in the high energy +− binding, splits into two additional steps. In the first step, a dipolar structures is generated next to the +− binding. In the second step, a negative charge of the dipolar structure

fuse with one of the positive charges of the the +− binding. Such fusion results in the dissolution of the dipolar structure and the +− binding, and the formation of a pair of separate half-strength defects with positive charges $s = 1/2$. As a result of these is two steps the high tension +− binding structurally diffuse into a configuration containing two positive half-strength defects. The rest of the transition steps 2 and 3 stay the same.

The existence of more than four half-strength defects in the nematic state has been also reported by Bates in ref. 67, where the excess defects were regarded as metastable structures. Our simulation results, however, show that additional defects form dipolar structures with zero charge and strongly interact with other single or bound defects. We distinguish between high density (HDDS) and low density (LDDS) dipolar structures. The HDDS, a representative picture of which is shown in Fig. 9 line 7, usually appears in high density $\eta = 0.85$ nematics in the proximity of the +− bindings and helps to relieve the strain of that binding. This is similar to the lining of many defects into scars in the Thompson problem.[16,68] At low η, the HDDS and the +− binding tend to fuse together with the ensuing unbinding of the positive half-strength defects and the annihilation of the dipolar structure. The LDDS, however, usually appears in low density nematics near the N–I transition line and in the vicinity of positive half-strength defects. It has a potential to increase the structural diffusion of the defect by absorbing the defect as a new cap, and releasing its old cap as a new half-strength defect. This mechanism is similar to the defect motion in crystalline solids.[64–66] In total, the dipolar structures are the essential part of the morphology observed in ordered liquids placed on compact surfaces.

As seen from Fig. 8a and b, there are similar high density states with the same defect structures, which, however, have developed from different initial configurations. For example, the iso-cap smectic state $0S_{000}^{002}$ at $\eta = 0.85$ and $L = 4$ can exist either in the splay-like orientation of the rods, or in the bending-like orientation of the rods at the equator, see Fig. 8a, respectively. Similarly, the nematic states $4N_{200}^{000}$ in Fig. 8a, and $4N_{020}^{000}$ in Fig. 8b corresponding to $\eta = 0.85$ and $L = 20$, differ from each-other only by the morphology of the defect bindings. In order to detect which of these alike states is a configuration with the lowest free energy, both alike systems were shrunk the continuously through the decreasing of R. It was found that the states with the splay-like deformation always endure more shrinking. Therefore, for $\eta = 0.85$ the more stable configurations are in the states shown in Fig. 8a. We note that the system pressure P can also be calculated using the virial theorem and moment transfer between particles per unit time.[56,60,69–71]

8 Conclusions

In conclusion, we explored topological structures of spherocylinders on a spherical surface in particular when they are in the smectic state. We found several exotic topological states which are highly nontrivial structures and are controlled by the imprinted orientational pattern, by the sphere radius and the spherocylinder aspect ratio and density. These exotic structures include a broken egg-shell like modulated smectic shown in Fig. 4 line 2, equatorial smectic with empty poles shown in Fig. 7 line 3, equatorial smectic with isotropic poles shown in Fig. 9 line 4, a capped nematic with equatorial bald patches shown in Fig. 4 line 4, equatorial nematic with empty poles shown in Fig. 7 line 5, and a situation with more than 4 half-strength topological defects shown in Fig. 9 lines 3 and 7. We expect that the topology of these structures is general and independent on the specific shape of the rods. Some of these structures can grow only in a very high density nematics generated in specifically tailored simulations with the bottom up architecture.

We found that there are stable smectic states at low curvatures L/R and high packing fractions $\eta = 0.9$. The topological structures of these smectics have four half-strength defects which form a +− binding structure at the poles. At large curvatures L/R the stable state appears to be high density nematics with the same four half-strength defects at the poles. However, in this case the defects form a ++ binding structure.

A detailed analysis of the exotic 8 half-strength topologies showed that the additional 4 half-strength defects create 2 dipolar defect structures of zero charge. We have detected that the high density dipolar structures appear next to the high density +− defect bindings and help to relieve the strain of these bindings. In this way they behave like the defect scars in the Thompson problem.[16] On the other hand, the low density dipolar structures appear near the N–I transition line and next to the single disclinations. They might enhance the structural diffusion of the defect by absorbing the disclination as a new cap, and releasing its own cap as a new half-strength disclination, a mechanism strongly resembling the defect motion in crystalline solids[65] and the Grotthuss hopping of protons in water.[72] In both cases the dipolar structures exert elastic torques on the disclinations and strongly contribute to their orientational mechanics.[22,73] In this sense, it will be interesting to analyze the role of the dipolar structures in active nematics placed on a spherical surface. In ref. 73–75 it is shown that the disclinations act as local sources of motion in 2D active nematics. An open question then remains, how the dipolar structures and their interaction with the disclinations will affect the morphology of the active nematics.

The structural diffusion of the positive half-strength defects guided by the dipolar structures reported in this work, can be assumed as a directional move from the poles towards the equator in high density systems. This directed strain-driven diffusion resembles the field driven directed motion of skyrmions, the topological vortex-like defects in chiral nematic liquid crystals under applied alternation current voltages.[76] The location and structural diffusion of the defects can be visualized by the fluorescent carbon dot nanoparticles which tend to accumulate at the cores of the topological defects.[77,78] Here it is important to note that, unlike the defect diffusion, which is only structural without any physical displacement of the spherocylinder on the S_2, the migration of the nanoparticles will be a

real transport. This will provide easy experimental verification of the defect dynamics on the the spherical surface.[79,80]

Our results pave the way towards possible applications of the structures found. In fact, steering the morphology of liquid crystalline shells is important for constructing switchable capsules optimal for a controlled drug delivery[81] where the defect positions determine where the shells can be opened in a minimal destructive way. Moreover, smectic shells with 4 integer defects are possible candidates to form supramolecular building blocks for tetrahedral crystals with important implications for photonics.[82] They can also been used for producing super-stable foams.[83] The discovered exotic states with particle-free areas, such as equatorial smectic with empty poles, equatorial nematic with empty poles, and a capped nematic with equatorial bald patches, are promising structures as building blocks for composite soft matter. The construction of new metamaterials based on these topologies remains as an interesting future research line.

Conflicts of interest

There are no conflicts to declare.

Appendix

A Free energy of the ordered state

For the system of N hard-core spherocylinders of length L and diameter D in a fixed volume V at a fixed temperature T, the corresponding ensemble is the canonical ensemble, and the corresponding thermodynamic potential is the Helmholtz free energy, $F(N,T,V)$. Under the equilibrium condition with no particle overlappings and no external potential, the free energy F has the following three contributions,

$$F = F_{\mathrm{id}}[\rho(\vec{r})] + F_{\eta}[\rho(\vec{r})] + F_{\alpha}[\rho(\vec{r})] \tag{A1}$$

The particle density $\rho(\vec{r}) = \left\langle \sum_{i=1}^{N} \delta(\vec{r} - \vec{r}_i) \right\rangle$ is assumed homogeneous everywhere, $\rho(\vec{r}) = N/V = \rho$. The first term in eqn (A1) is the Helmholtz free energy of the ideal gas of rods,

$$\frac{F_{\mathrm{id}}}{Nk_{\mathrm{B}}T} = \ln\left(\rho\Lambda^3\right) - 1 \tag{A2}$$

where k_{B} is the Boltzmann's constant, Λ is the thermal De-Broglie wavelength, $\Lambda = h/\sqrt{2\pi m k_{\mathrm{B}}T}$,

The second term in eqn (A1) is associated with the excluded volume interaction between particles, and in the limit of low densities is given as

$$\frac{F_{\eta}}{Nk_{\mathrm{B}}T} = \rho L^2 D \int f\left(\hat{\Omega}_1\right) f\left(\hat{\Omega}_2\right) \langle |\sin\gamma| \rangle \mathrm{d}\hat{\Omega}_1 \mathrm{d}\hat{\Omega}_2 + 4\eta \tag{A3}$$

where $\eta = \rho(\pi D^2 L/4 + \pi D^3/6)$ is the packing fraction of the spherocylinders, $\mathrm{d}\hat{\Omega} = \sin\theta \mathrm{d}\theta \mathrm{d}\varphi$ denotes a surface element spanning from θ to $\theta + \mathrm{d}\theta$ and φ to $\varphi + \mathrm{d}\varphi$ on a spherical surface of unit sphere, $f(\hat{\Omega})$ is the orientational distribution function (ODF) normalized as $\int f(\hat{\Omega})\mathrm{d}\hat{\Omega} = 1, \gamma\left(\hat{\Omega}_1, \hat{\Omega}_2\right) = \arccos(\cos\theta_1\cos\theta_2 + \sin\theta_1\sin\theta_2\cos(\varphi_1 - \varphi_2))$ is the angle between the rods which depends on their orientations $\hat{\Omega}_1$ and $\hat{\Omega}_2$, and $\langle \cdots \rangle$ is the statistical averaging over all mutual orientations for the rod pairs. The term $-F_{\eta}/T$ is regarded as the positional entropy term for the rods.

The third term in eqn (A1) is associated with the orientational entropy loss in the nematic phase compared to the isotropic phase and has the following form

$$\frac{F_{\alpha}}{Nk_{\mathrm{B}}T} = \int f(\hat{\Omega}) \ln\left[4\pi f(\hat{\Omega})\right] \mathrm{d}\hat{\Omega} \tag{A4}$$

Here the parameter α represents the degree of alignment of the spherocylinder.

The thermodynamic equilibrium of the system of N spherocylinders corresponds to the minimum of the free energy F over the parameter f. From the several trial functions proposed for f[84–86] the Gaussian form seems to be a more convenient choice,

$$f(\alpha,\theta) = C(\alpha)\exp\left(-\frac{1}{2}\alpha\theta'^2\right) \tag{A5}$$

Here $C(\alpha)$ is the normalization factor and $C(\alpha) \approx \alpha$ for larger α, and $\theta' = \theta$ for $0 \le \theta \le \pi/2$, and $\theta' = \pi - \theta$ for $\pi/2 \le \theta \le \pi$. Putting the Gaussian ODF into eqn (A3) and (A4), we get for the the free energy parts the following expressions,

$$\frac{F_{\eta}^{\mathrm{G}}}{Nk_{\mathrm{B}}T} = \frac{\pi\rho_0 L^2 D}{\sqrt{\pi\alpha}} + 4\eta, \quad \frac{F_{\alpha}^{\mathrm{G}}}{Nk_{\mathrm{B}}T} = \ln\alpha - 1 \tag{A6}$$

It is obvious that F_{η}^{G} is a monotonically decreasing function of α, whereas F_{α}^{G} is a monotonically increasing function of α. The competition between the increase in the positional entropy $-F_{\eta}/T$ and the loss of the orientational entropy $-F_{\alpha}/T$ minimizes the total free energy F of the system of rods and drives the system into a nematic phase at sufficiently high η. At low η, in the isotropic phase with $\alpha = 0$, $f = 1/(4\pi)$, and thus $\langle |\sin\gamma| \rangle = \int\int \sin\gamma \mathrm{d}\hat{\Omega}_1 \mathrm{d}\hat{\Omega}_2 = \pi/4$. In this case, according to eqn (A3) and (A4), $F_{\eta}^{\mathrm{I}}/(Nk_{\mathrm{B}}T) = \pi\rho_0 L^2 D/4 + 4\eta$, and $F_{\alpha}^{\mathrm{I}} = 0$.

B Defect structures in nematics

On compact 2D surfaces (spheres, ellipsoids, *etc.*) each defect is defined by its topological charge s corresponding to the change of the director $\vec{n}$ when a full revolution of 2π is done around the defect, and the angular phase parameter γ_s. The latter is defined as the angle between the radius vector $\vec{r} = \vec{r}_i - \vec{r}_s$ of the point $\vec{r}_i$ near the defect and the director $\vec{n}$ at this point, $\cos(\gamma_s) = \vec{r}\cdot\vec{n}/rn$. A set of six fundamental and low-energy defect structures on compact 2D surfaces is schematically illustrated in Fig. 10. There are four full defects $|s| = 1$ and 2 half defects $|s| = 1/2$. The phase parameter γ_s regulates the transition from a purely splay-like defect ($s = 1$, $\gamma_s = 0$, $K_3 \gg K_1$) to a purely bending-like defect ($s = 1$, $\gamma_s = \pi/2$, $K_1 \gg K_3$), which can be induced by the external fields.[52]

Under equilibrium conditions the energy of the full strength defect is higher than the summarized energy of the two half-strength defects.[87] As a result of this, the $|s| = 1$ defect tends to split into a pair of $|s| = 1/2$ disclinations schematically shown in Fig. 11. As seen from this figure, the local direction field $\vec{n}$ lines between the half-strength defects resemble electric field lines

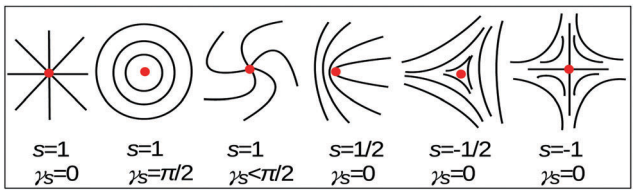

Fig. 10 Defect inclinations on compact 2D surfaces with corresponding topological charge s and phase γ_s parameters.

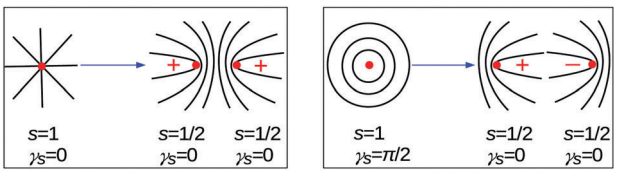

Fig. 11 Splitting of splay-like (left picture) and bending-like (right picture) full defects into two half-strength defects.

between likewise charged (left picture in Fig. 11), or between oppositely charged (right picture in Fig. 11) particles. We will refer to these configurations as the ++ and +− binding of the half-strength defects. The total charge of all defects $\chi = \sum_i s_i = 2$ on the compact surface S_2 is a topological invariant.[88–90] This corresponds to either a pair of $s = 1$ defects at the geometrical poles of the sphere, or to a pattern of four $s = 1/2$ defects on S_2. At low η this pattern coincides with the vertices of a regular tetrahedron with a baseball-like nematic texture.[47,50,91] At high η the four defects are found to lie on a great circle[92–95] forming cut and rotate morphology.

There is an interesting analogy between the defects with $\chi = 2$ on S_2 and the 12 defects in the triangular lattice created by the mutually repulsive discs placed on S_2.[96] In the latter case each defect has 5 neighbors (a pentamer) instead of 6 neighbors (a hexamer) expected in a defect-free triangular lattice.[97] The lack of 1 neighbor at each defective pentamer is equivalent to having $2\pi/6$ angular increment (or 1/6 "charge") per pentamer. Thus, all the 12 defects of the triangular lattice on the sphere will have the same topological charge $\chi = 2$ as the spherocylinders on S_2.

For the discs on S_2 it is also known that at larger number of particles additional 5–7 (pentamer–heptamer) pairs form defect scars in the vicinity of the original pentamer defect. The scar has zero topological charge and reduces the tension around the pentamer defect.[16,98] A similar observation, an existence of more than four half-strength defects on the S_2 in spherocylinder system has been made in ref. 67. The total charge of the extra disclinations is also zero.

Acknowledgements

We thank F. Smallenburg (HHU Düsseldorf) and P. L. Taylor (CWRU Cleveland) for helpful discussions. E. A. also thanks A. Rukhadze, A. Ignatov, and N. Guseinzade (GPI RAS Moscow) for their valuable comments during the presentation of this work. We are thankful for support of this work by the Deutsche Forschungsgemeinschaft (DFG) through the grants AL 2058/1-1 (for E. A.), LO 418/20-1 (for H. L.), and VO 899/19-1 (for A. V.)

References

1 T. N. Shendruk and J. M. Yeomans, *Soft Matter*, 2015, **11**, 5101–5110.
2 L. Tortora, H.-S. Park, S.-W. Kang, V. Savaryn, S.-H. Hong, K. Kaznatcheev, D. Finotello, S. Sprunt, S. Kumar and O. D. Lavrentovich, *Soft Matter*, 2010, **6**, 4157–4167.
3 D. S. Kim, Y. J. Cha, M. H. Kim, O. D. Lavrentovich and D. K. Yoon, *Nat. Commun.*, 2016, **7**, 10236.
4 R. van Roij, P. Bolhuis, B. Mulder and D. Frenkel, *Phys. Rev. E: Stat. Phys., Plasmas, Fluids, Relat. Interdiscip. Top.*, 1995, **52**, R1277–R1280.
5 S. Belli, M. Dijkstra and R. van Roij, *J. Chem. Phys.*, 2012, **137**, 124506.
6 D. Frenkel and B. Smit, *Understanding Molecular Simulation*, Academic Press, 2002.
7 P. M. Chaikin and T. C. Lubensky, *Principles of Condensed Matter Physics*, Cambridge University Press, 1995.
8 J. M. Harris, R. Lindquist, J. Rhee and J. E. Webb, *Liquid-Crystal Based Optical Switching*, Springer US, Boston, MA, 2006, pp. 141–167.
9 A. J. C. Wilson, *Molecular Structure and the Properties of Liquid Crystals*, Academic Press, 1962, vol. 15, p. 922.
10 P. Bolhuis and D. Frenkel, *J. Chem. Phys.*, 1997, **106**, 666–687.
11 M. A. Bates and D. Frenkel, *J. Chem. Phys.*, 2000, **112**, 10034.
12 A. Martinez, M. Ravnik, B. Lucero, R. Visvanathan, S. Zumer and I. I. Smalyukh, *Nat. Mater.*, 2014, **13**, 258–263.
13 T. Araki, F. Serrab and H. Tanaka, *Soft Matter*, 2013, **9**, 8107–8120.
14 T. Araki, M. Buscaglia, T. Bellini and H. Tanaka, *Nat. Mater.*, 2011, **10**, 303–309.
15 H. Stark, *Phys. Rep.*, 2001, **351**, 378–474.
16 A. R. Bausch, M. J. Bowick, A. Cacciuto, A. D. Dinsmore, M. F. Hsu, D. R. Nelson, M. G. Nikolaides, A. Travesset and D. A. Weitz, *Science*, 2003, **299**, 1716–1718.
17 P. Poulin, H. Stark, T. C. Lubensky and D. A. Weitz, *Science*, 1997, **275**, 1770–1773.
18 J. Dzubiella, M. Schmidt and H. Löwen, *Phys. Rev. E: Stat. Phys., Plasmas, Fluids, Relat. Interdiscip. Top.*, 2000, **62**, 5081–5091.
19 M. A. Bates, G. Skacej and C. Zannoni, *Soft Matter*, 2010, **6**, 665–670.
20 H. Shin, M. J. Bowick and X. Xing, *Phys. Rev. Lett.*, 2008, **101**, 037802.
21 M. M. Genkin, A. Sokolov, O. D. Lavrentovich and I. S. Aranson, *Phys. Rev. X*, 2017, 7, 011029.
22 A. J. Vromans and L. Giomi, *Soft Matter*, 2016, **12**, 6490–6495.
23 M. Schoen, T. Gruhn and D. J. Diestler, *J. Chem. Phys.*, 1998, **109**, 301–311.

24 C. Knorowski and A. Travesset, *Europhys. Lett.*, 2012, **100**, 56004.
25 R. A. Mosna, D. A. Beller and R. D. Kamien, *Phys. Rev. E: Stat., Nonlinear, Soft Matter Phys.*, 2012, **86**, 011707.
26 X. Xing, H. Shin, M. J. Bowick, Z. Yao, L. Jia and M.-H. Li, *Proc. Natl. Acad. Sci. U. S. A.*, 2012, **109**, 5202–5206.
27 P. G. de Gennes and J. Prost, *The Physics of Liquid Crystals*, 2nd edn, Oxford Science Publications, 1993.
28 F. Smallenburg and H. Löwen, *J. Chem. Phys.*, 2016, **144**, 164903.
29 V. Koning, T. Lopez-Leon, A. Fernandez-Nieves and V. Vitelli, *Soft Matter*, 2013, **9**, 4993–5003.
30 A. Fernandez-Nieves, V. Vitelli, A. S. Utada, D. R. Link, M. Marquez, D. R. Nelson and D. A. Weitz, *Phys. Rev. Lett.*, 2007, **99**, 157801.
31 T. Lopez-Leon, A. Fernandez-Nieves, M. Nobili and C. Blanc, *J. Phys.: Condens. Matter*, 2012, **24**, 284122.
32 H. L. Liang, J. Noh, R. Zentel, P. Rudquist and J. P. F. Lagerwall, *Philos. Trans. R. Soc., A*, 2013, **371**, 20120258.
33 H. L. Liang, S. Schymura, P. Rudquist and J. Lagerwall, *Phys. Rev. Lett.*, 2011, **106**, 247801.
34 K. May, K. Harth, T. Trittel and R. Stannarius, *Europhys. Lett.*, 2012, **100**, 16003.
35 K. May, K. Harth, T. Trittel and R. Stannarius, *ChemPhysChem*, 2014, **15**, 1508–1518.
36 J. P. F. Lagerwall, C. Schütz, M. Salajkova, J. H. Noh, J. H. Park, G. Scalia and L. Bergström, *NPG Asia Mater.*, 2014, **6**, e80.
37 A. Eremin, S. Baumgarten, K. Harth, R. Stannarius, Z. H. Nguyen, A. Goldfain, C. S. Park, J. E. Maclennan, M. A. Glaser and N. A. Clark, *Phys. Rev. Lett.*, 2011, **107**, 268301.
38 S. Dölle and R. Stannarius, *Langmuir*, 2015, **31**, 6479–6486.
39 R. Stannarius and K. Harth, *Phys. Rev. Lett.*, 2016, **117**, 157801.
40 L. Jia, A. Cao, D. Lévy, B. Xu, P.-A. Albouy, X. Xiangjun, M. J. Bowick and M.-H. Li, *Soft Matter*, 2009, **5**, 3446–3451.
41 B. Xu, R. Pinol, M. Nono-Djamen, S. Pensec, P. Keller, P.-A. Albouy, D. Lévy and M.-H. Li, *Faraday Discuss.*, 2009, **143**, 235–250.
42 L. Jia, D. Lévy, D. Durand, M. Imperor-Clerc, A. Cao and M.-H. Li, *Soft Matter*, 2011, **7**, 7395–7403.
43 W. Zhou, J. Cao, W. Liu and S. Stoyanov, *Angew. Chem., Int. Ed.*, 2009, **48**, 378–381.
44 H. Yu and K. Schulten, *Comput. Biol.*, 2013, **9**, e1002892.
45 H. Noguchi, *Sci. Rep.*, 2016, **6**, 20935.
46 X. Li, B. Caswell and G. E. Karniadakis, *Biophys. J.*, 2012, **103**, 1130–1140.
47 D. R. Nelson, *Defects and Geometry in Condensed Matter Physics*, Cambridge University Press, 2002.
48 T. Lopez-Leon, A. Fernandez-Nieves, M. Nobili and C. Blanc, *Phys. Rev. Lett.*, 2011, **106**, 247802.
49 T. Lopez-Leon, V. Koning, K. B. S. Devaiah, V. Vitelli and A. Fernandez-Nieves, *Nat. Phys.*, 2011, **7**, 391–394.
50 D. R. Nelson, *Nano Lett.*, 2002, **2**, 1125–1129.
51 G. A. Devries, M. Brunnbauer, Y. Hu, A. M. Jackson, B. Long, B. T. Neltner, O. Uzun, B. H. Wunsch and F. Stellacci, *Science*, 2007, **315**, 358–361.
52 T. Lopez-Leon and A. Fernandez-Nieves, *Colloid Polym. Sci.*, 2011, **289**, 345–359.
53 M. P. Taylor, R. Hentschke and J. Herzfeld, *Phys. Rev. Lett.*, 1989, **61**, 800–803.
54 H. N. W. Stroobants, A. Lekkerkerker and D. Frenkel, *Phys. Rev. A: At., Mol., Opt. Phys.*, 1987, **36**, 2929–2945.
55 C. Vega and S. Lago, *Comput. Chem.*, 1994, **18**, 55–59.
56 D. W. Rebertus and K. M. Sando, *J. Chem. Phys.*, 1977, **67**, 2585–2590.
57 W. H. de Jeu, B. I. Ostrovskii and A. N. Shalaginov, *Rev. Mod. Phys.*, 2003, **75**, 182–239.
58 R. Tavarone, P. Charbonneau and H. Stark, *J. Chem. Phys.*, 2015, **143**, 114505.
59 J. Polson and D. Frenkel, *Phys. Rev. E: Stat. Phys., Plasmas, Fluids, Relat. Interdiscip. Top.*, 1997, **56**, R6260–R6263.
60 E. Fischermeier, D. Bartuschat, T. Preclik, M. Marechal and K. Mecke, *Comput. Phys. Commun.*, 2014, **185**, 3156–3161.
61 M. P. Allen and D. Frenkel, *Phys. Rev. A: At., Mol., Opt. Phys.*, 1988, **37**, 1813–1816.
62 T. Araki and H. Tanaka, *Phys. Rev. Lett.*, 2006, **97**, 127801.
63 X. Duan and Z. Yao, *Phys. Rev. E*, 2017, **95**, 062706.
64 T. Angsten, T. Mayeshiba, H. Wu and D. Morgan, *New J. Phys.*, 2014, **16**, 015018.
65 L. N. McCartney, *Acta Metall.*, 1975, **23**, 769–777.
66 G. E. Murch, *Simulation of Diffusion Kinetics with the Monte Carlo Method*, Academic Press, 1984, pp. 379–427.
67 M. A. Bates, *Soft Matter*, 2008, **4**, 2059–2063.
68 M. J. Bowick and L. Giomi, *Adv. Phys.*, 2009, **58**, 449–563.
69 E. Allahyarov, I. D'Amico and H. Löwen, *Phys. Rev. Lett.*, 1998, **81**, 1334–1337.
70 M. N. Bannerman, L. Lue and L. V. Woodcock, *J. Chem. Phys.*, 2010, **132**, 084507.
71 J. J. Erpenbeck and W. W. Wood, *J. Stat. Phys.*, 1984, **35**, 321–340.
72 N. Agmon, *Chem. Phys. Lett.*, 1995, **244**, 456–462.
73 L. Giomi, M. J. Bowick, P. Mishra, R. Sknepnek and M. C. Marchetti, *Philos. Trans. R. Soc., A*, 2014, **372**, 20130365.
74 S. J. DeCamp, G. S. Redner, A. Baskaran, M. F. Hagan and Z. Dogic, *Nat. Mater.*, 2015, **14**, 1110–1115.
75 E. Putzig, G. S. Redner, A. Baskaran and A. Baskaran, *Soft Matter*, 2016, **12**, 3854–3859.
76 P. J. Ackerman, T. Boyle and I. I. Smalyukh, 2017, arXiv:1706.09514, cond-mat.mtrl-sci, pp. 1–36.
77 D. Coursault, J. Grand, B. Zappone, H. Ayeb, G. Lévi, N. Félidj and E. Lacaze, *Adv. Mater.*, 2012, **24**, 1461–1465.
78 I. Musevic, M. Skarabot, U. Tkalec, M. Ravnik and S. Zumer, *Science*, 2006, **313**, 954–958.
79 J. K. Whitmer, X. Wang, F. Mondiot, D. S. Miller, N. L. Abbott and J. J. de Pablo, *Phys. Rev. Lett.*, 2013, **111**, 227801.
80 M. Rahimi, T. F. Roberts, J. C. Armas-Pérez, X. Wang, E. Bukusoglu, N. L. Abbott and J. J. de Pablo, *Proc. Natl. Acad. Sci. U. S. A.*, 2015, **112**, 5297–5302.
81 S. A. Jenekhe and X. L. Chen, *Science*, 1998, **279**, 1903–1907.
82 D. Zerrouki, B. Rotenberg, S. Abramson, J. Baudry, C. Goubault, F. Leal-Calderon, D. J. Pine and J. Bibette, *Langmuir*, 2006, **22**, 57–62.

83 B. P. Binks, *Curr. Opin. Colloid Interface Sci.*, 2002, **7**, 21–41.
84 R. Tuinier, *Adv. Condens. Matter Phys.*, 2016, **2016**, 1–6.
85 L. Onsager, *Ann. N. Y. Acad. Sci.*, 1949, **51**, 627–659.
86 G. J. Vroege and H. N. W. Lekkerkerker, *Rep. Prog. Phys.*, 1992, **55**, 1241–1309.
87 J. M. Kosterlitz and D. Thouless, *J. Phys. C: Solid State Phys.*, 1973, **6**, 1181–1203.
88 H. Poincaré, *J. Math. Pures Appl.*, 1885, **1**, 167–244.
89 H. Hopf, *Math. Ann.*, 1927, **96**, 225–249.
90 O. Bonnet, *J. Ec. Polytech.*, 1848, **19**, 1–146.
91 T. C. Lubensky and J. Prost, *J. Phys. II*, 1992, **2**, 371–382.
92 M. A. Bates, *J. Chem. Phys.*, 2008, **128**, 104707.
93 H. Shin, M. J. Bowick and X. Xing, *Phys. Rev. Lett.*, 2008, **101**, 037802.
94 Q. Liang, S. Ye, P. Zhang and J. Z. Y. Chen, *J. Chem. Phys.*, 2014, **141**, 244901.
95 S. Dhakal, F. J. Solis and M. O. de la Cruz, *Phys. Rev. E: Stat., Nonlinear, Soft Matter Phys.*, 2012, **86**, 011709.
96 M. Henle, *A Combinatorial Introduction to Topology*, Dover, 1979.
97 E. L. Altschuler, T. J. Williams, E. R. Ratner, R. Tipton, R. Stong, F. Dowla and F. Wooten, *Phys. Rev. Lett.*, 1997, **78**, 2681–2685.
98 P. Lipowsky, M. J. Bowick, J. H. Meinke, D. R. Nelson and A. R. Bausch, *Nat. Mater.*, 2005, **4**, 407–411.